Virtually measuring layered material appearance

Kewei Xu, Arthur Cavalier, Benjamin Bringier, Mickaël Ribardière, Daniel Meneveaux

▶ **To cite this version:**

Kewei Xu, Arthur Cavalier, Benjamin Bringier, Mickaël Ribardière, Daniel Meneveaux. Virtually measuring layered material appearance. Journal of the Optical Society of America. A Optics, Image Science, and Vision, 2024, 41 (5), pp.959. 10.1364/JOSAA.514604 . hal-04676050

HAL Id: hal-04676050
https://hal.science/hal-04676050v1

Submitted on 28 Nov 2024

HAL is a multi-disciplinary open access archive for the deposit and dissemination of scientific research documents, whether they are published or not. The documents may come from teaching and research institutions in France or abroad, or from public or private research centers.

L'archive ouverte pluridisciplinaire **HAL**, est destinée au dépôt et à la diffusion de documents scientifiques de niveau recherche, publiés ou non, émanant des établissements d'enseignement et de recherche français ou étrangers, des laboratoires publics ou privés.

Virtually Measuring Layered Material Appearance

KEWEI XU[1], ARTHUR CAVALIER[1], BENJAMIN BRINGIER[1], MICKAËL RIBARDIÈRE[1], AND DANIEL MENEVEAUX[1]

[1] University of Poitiers - XLIM
[*] Corresponding author: kewei.xu@univ-poitiers.fr

This paper describes the design and the implementation of a virtual gonioradiometer dedicated to the analysis of layered materials BSDF. For a given material sample, interfaces between layers are represented by geometric meshes, associated with elementary reflectances. Light scattering is performed using path tracing. Our system is composed of 5 hemispherical sensors, which cells have uniform solid angles, and a close-to-uniform geometry. The upper hemisphere captures the reflected radiance distribution, while the other 4 collect the light energy lost by the sample sides. Sensor resolutions can be set to gather very fine details of the BSDF. With the proposed system, any type of virtual surface reflection and transmission can be simulated, with several controllable surface layers, and with any type of reflection configuration, including direct reflections, two bounces of reflection, or all contributions. A series of results are provided with several types of layered materials, as well as discussion and analysis concerning the assumptions made with analytical layered BSDF models. We also propose an in-depth study of the side effects that inevitably appear when measuring such (real) material configurations. Finally, our system will be freely available to the community (open source dissemination).

1. INTRODUCTION AND RELATED WORK

Understanding materials' appearance is required for many design applications, including for instance 3D printing and fabrication, physics material analysis, surface prototyping, or physically-based rendering. The BSDF (*Bidirectional Scattering Distribution Function*) describes the physical and directional aspects of material appearance. It can be represented either by measurements of real material samples using gonioradiometers, or by analytical predictive models.

Material measurement can be considered as a ground truth, but their acquisition requires complex experimental tools, hard to implement, and the acquisition process may require several hours (even for low resolution sampling) and it may be prone to measurement errors or unreliability, especially at grazing angles (lighting and observation). Such systems often require a specific management for complex materials, for instance when dealing with multi-layer materials or surfaces covered by a liquid.

Many predictive models have been proposed in the literature, but each of them only represents a small subset of the whole existing range of material appearances. Among those, microfacet models are nowadays considered as the most versatile and closest-to-reality since they are built upon physical considerations and rigorous mathematical developments. According to these models, a BSDF $f(\mathbf{i},\mathbf{o},\mathbf{n})$ relies on a statistical distribution of microfacets organization. The general equation is given by [1, 2]:

$$f(\mathbf{i},\mathbf{o},\mathbf{n}) = \int_{\Omega_+} \frac{|\mathbf{i}\cdot\mathbf{m}|}{|\mathbf{i}\cdot\mathbf{n}|} f^{\mu}(\mathbf{i},\mathbf{o},\mathbf{m}) \frac{|\mathbf{o}\cdot\mathbf{m}|}{|\mathbf{o}\cdot\mathbf{n}|} D(\mathbf{m}) G(\mathbf{i},\mathbf{o},\mathbf{m}) d\omega_m, \quad \textbf{(1)}$$

where $f^{\mu}(\mathbf{i},\mathbf{o},\mathbf{m})$ is the elementary BSDF of an individual microfacet associated with its normal vector $\mathbf{m}$. Each contribution is weighted by the distribution $D(\mathbf{m})$ and a geometric attenuation factor $G(\mathbf{i},\mathbf{o},\mathbf{m})$. $D(\mathbf{m})$ is the Normal Distribution Function (NDF), that defines the surface roughness, indicating the proportion of microfacets corresponding to a normal $\mathbf{m}$; $G(\mathbf{i},\mathbf{o},\mathbf{m})$ expresses the portion of a microfacet of normal $\mathbf{m}$ visible from both the light source and the observer. Many authors have studied the combinations of distributions and geometric attenuation factors [1, 3–10], which have to be carefully chosen together [6, 11]. Usually, Smith assumptions are considered as the most realistic [12] for G [2, 13]. Note that Equation 1 expresses the reflectance that corresponds to a single bounce of light reflection only (attenuated thanks to G). It neglects light multiple scattering effects. Unfortunately, such statistical descriptions, even with versatile NDFs as GGX [2] or Student-T [10], combined with their proper Smith formulations, do not often correspond to measured real surface reflectance.

Zhu et al. [14] propose a complete review dedicated to radiative properties of rough surfaces, including geometric and wave optics simulations. Layered materials even drastically increase

these constraints and limitations. This is why recent research neglects thickness between each layer's interface [15–20] for deriving analytical dedicated models. The comparison between such models and real measurements remains a complex issue. In practice, configurations with a liquid spread over a solid surface for instance would be hard to measure because the liquid layer could not be controlled and stabilized over the surface without placing the whole sample in a (transparent) box, biasing measurements. Several authors have proposed to study virtual measurements of the appearance corresponding to multi-layered materials [21, 22], based on lighting simulation [23]. However, to the best of our knowledge none of them has addressed the light energy that exits by samples sides; the measurements lead by previous authors do not consider the light energy lost by the sample sides. This article proposes a complete virtual gonioradiometer system dedicated to the understanding and the prediction of the reflected/transmitted energy distribution. As an example, we propose to study layered material samples and illustrate the light energy that leaves the material by the sides, thanks to numerical lighting simulation. It is free from physical constraints but compliant with microfacet theory, allowing to study any material appearance assumptions, without any restriction on multiple scattering effects nor surface topology. We first relax statistical formulations, using explicit surface description with triangular meshes, obtained from any surface acquisition process (laserometry, photometric stereo process, photogrammetric techniques, etc.). Using overlaying meshes, our framework is able to represent complex multi-layered material configurations with complex light scattering. Our gonioradiometer system performs path tracing simulation through the virtual material sample. The reflected light flux is then captured by a hemispherical sensor. Energy loss, due to edge effects on the border of the material sample (Figure 1-[b-2]), is also captured by spatial and directional sensors.

Our virtual gonioradiometer allows us to better understand the complexity of real layered materials measurements. It can be employed for prototyping materials, with an opaque smooth or rough substrate, covered with several flat or rough translucent layers. Figure 1 illustrates the hemispherical sensor and the lighting simulation process. The main contributions of this paper are the following:

- definition of a complete layered BSDF simulation framework built upon a physically-based path tracing system that allows us to estimate of several types of contributions as often mentioned in the literature (single bounce denoted as L_1 in the following, two and more bounces denoted as L_{2+});
- design of a sensor which captures both the BSDF of the multi-layered material and the energy loss due to edge effects;
- in-depth analysis of these effects and their impact on the BSDF compared to multi-layered analytical models and their assumptions;
- management of any type of opaque or layered materials defined by triangle meshes and elementary reflectance/transmission properties (Lambertian, dielectric, conductor, transparent, etc.);

We demonstrate the utility of this virtual acquisition system with several multi-layered virtual materials.

The remainder of this paper is organized as follows: Section 2 discusses the main aspects of sensor and material representations, including lighting simulation issues; Section 3 presents and analyzes a series of results for several material configurations; Section 4 concludes and discusses the future potentialities that can be developed from this system.

2. VIRTUAL GONIORADIOMETER

Virtual gonioradiometers have been used for long in computer graphics. Cabral et al. and Westin et al. [24, 25] propose to represent the captured BSDF using basis functions (spherical harmonics). This representation is however prone to ringing artifacts and does not allow to capture high-frequency BSDF. Krishnaswamy et al. [26] discuss the protocol to simulate BSDF measurements. They do not consider layered material and the employed hemispherical sensor is unequally sampled, resulting in non uniform light capture which results in bad measurement distribution [27–31].

Some models are also based on lighting simulation, with surfaces represented by planes associated with bump maps as normal distributions [32] or triangular mesh [33] that do not account for layered materials. Gondek et al. [34] propose to trace light paths through full microgeometry, defined as a substrate, filled with dielectric microspheres or square specular particules, handling thin films with wavelength representations and interferences. Light distribution is captured using a hierarchical geodesic sphere construction. Our contribution is rather aligned with work that consider statistical distributions of layered interfaces [35–38]. We specifically focus on the analysis of the energy loss due to edge effects, which has not been simulated nor studied so far.

Our virtual system mimics real gonioradiometers, while being free from physical and material constraints: the light source produces a mono-spectral band collimated beam and grazing angles become virtually manageable (the polar angle θ_i is from 0° to 90° without any restriction). Material samples are represented as a stack of triangular meshes, each representing an interface between two media (Section A), separated by a given thickness h (in mm).

The proposed gonioradiometer is designed with one main hemispherical sensor that gather light reflections. It is subdivided in equal-area cells [39] (i.e., iso-solid angle and same aspect ratio for all cells to mitigate acquisition bias). This configuration is well adapted for capturing the BRDF (*Bidirectional Reflection Distribution Function*) of opaque single-layer materials. However, with multi-layered materials, the layers' width leads to light energy loss through the sample sides. This paper focuses on such configurations. In order to capture the effects of the sample thickness on side energy loss, hemispherical sensors with the same definition are placed at each side of the material sample. They are associated with sensors that gather the spatial distribution of side-exiting light. The complete description of these sensors is provided in Subsection C. A collimated light beam illuminates the virtual material sample from a fixed direction, defined by spherical angles $\theta_i \in [0^\circ; 90^\circ]$ and $\varphi_i \in [0^\circ, 360^\circ]$ (Figure 1). All the incoming light is reflected or transmitted after one bounce (L_1), two bounces and more (L_{2+}). It is captured by one of the hemispherical sensors, reaching one of its cells. Light paths are built thanks to a path tracing technique (Subsection B). Note that we only consider geometric optics because light wavelength is regarded as small compared to the size of the micro-geometry. Phase difference between two points on the surface would require considering wave optics model; it is let to future work.

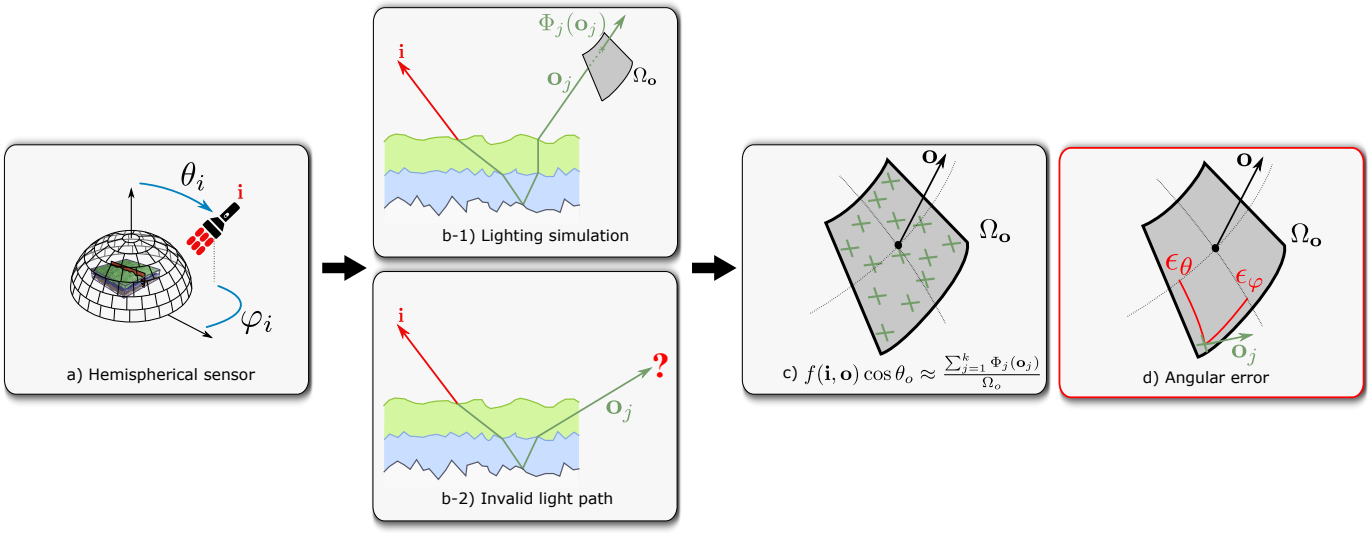

Fig. 1. a) Virtual gonioradiometer configuration with the upper hemispherical sensor; b-1) lighting simulation process, with path tracing; each light ray shot from incoming direction $\mathbf{i}$ propagates a flux through the layers; when it leaves the material it is captured by one sensor's cell; c) density estimation is performed for evaluating BSDF samples; d) for a sensor cell of solid angle $\Omega_\mathbf{o}$, the angular sampling bias ϵ_θ, ϵ_φ is known for each measured value; this bias decreases as the sensor's resolution increases; b-2) light beams may leave the material sample without crossing back the top layer interface, they are flagged as invalid and they are processed independently to evaluate the energy lost by the sample side.

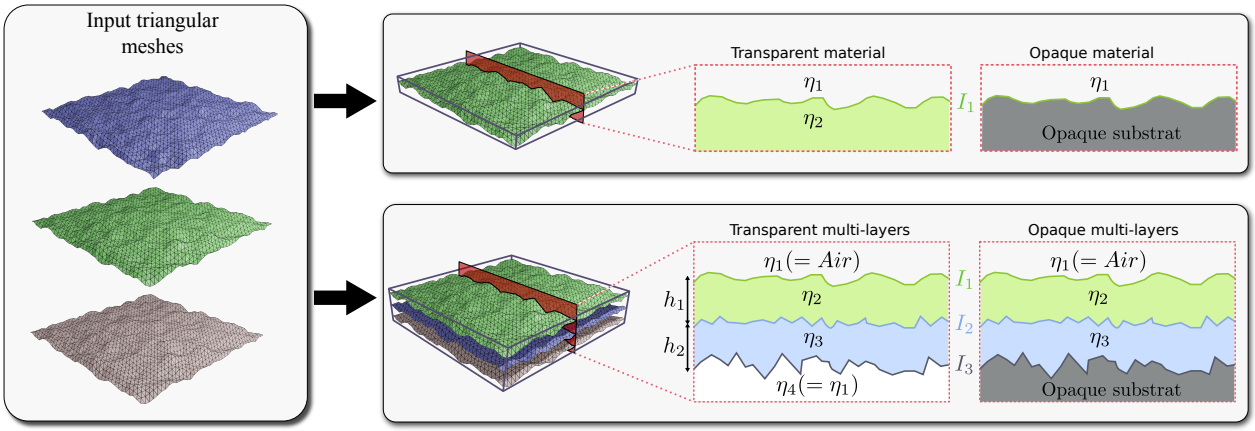

Fig. 2. Virtual material samples, opaque or transparent, are built from input triangular meshes: a single one for non-layered materials or several for multi-layered materials. Each mesh represents an interface I_n between two media described by their refractive index η_n, the lower interface corresponds to an opaque substratum (Lambertian or conductor) in the examples of this paper. Each interface I_n is separated from the next one by a thickness of h_n (in mm).

A. Material sample representation

A material sample is represented as a stack of triangular meshes, each of them defining the interface between two media (two layers). The first one represents the top of the stack, lit first by the collimated incoming beam. First and intermediate interfaces are necessarily transparent while the final one can be opaque or transparent. Our system can be obviously used with only one interface, opaque or transparent. Figure 2 illustrates this representation and introduces the notations used for layer components: interfaces, layers thickness (i.e. space between successive interfaces in mm) and medium refractive index.

Interfaces can be opaque (i.e. conductor or Lambertian diffuse surfaces) or transparent (i.e. dielectric surfaces). Transparent interfaces separate two media described by their index of refraction η while opaque ones come with their associated material parameters (e.g. albedo if the surface is Lambertian or refractive index for conductors), their layer thickness and their absorption coefficients. Digital geometries can be generated from different processes: manually built meshes without any constraints on the topology, procedurally derived from a Normal Distribution Function / height probability distribution [40, 41], or directly measured from real surfaces [42]. Most of these techniques build a heigthmap, then converted to a triangular mesh aligned with a regular grid. The conversion process is out of the scope of this paper, we consider the triangular meshes as the input data of our system, independently from the (re)construction

process.

Finally, all interfaces must have the same size on the XY tangent plane and their mean plane must be aligned on the macro-surface normal. In all the experiments conducted for this paper, material samples correspond to surfaces of $4\times4\text{mm}^2$. We performed a series of experiments that lead to this configuration that we considered as a good trade-off between memory and performance, without providing noisy results.

B. Monte Carlo path tracing - light propagation

Considering a couple of directions $(\mathbf{i},\mathbf{o})$ and their corresponding solid angles $(\omega_\mathbf{i},\omega_\mathbf{o})$, the BSDF of the micro-geometry $\mathcal{M}$ is defined as the ratio between the outgoing (reflected or transmitted) and the incoming light:

$$f(\mathcal{M},\mathbf{i},\mathbf{o}) = \frac{dL_o(\mathcal{M},\mathbf{o})}{dE(\mathcal{M},\mathbf{i})} = \frac{dL_o(\mathcal{M},\mathbf{o})}{L_i(\mathcal{M},\mathbf{i})\cos\theta_\mathbf{i} d\omega_\mathbf{i}} \tag{2}$$

where $dL_o(\mathcal{M},\mathbf{o})$ is the element of outgoing radiance from $\mathcal{M}$ in direction $\mathbf{o}$ only due to light coming from direction. A gonioradiometer evaluates the BSDF, *i.e.* the reflected contributions (and/or transmitted) from the top (and/or bottom) interface of the micro-geometry $\mathcal{M}$.

With our virtual system, the surface is illuminated from one fixed direction $\mathbf{i}$ at a time. The elementary outgoing radiance thus equals the global outgoing radiance $dL_o(\mathcal{M},\mathbf{o}) \rightarrow L_o(\mathcal{M},\mathbf{o})$, without any loss of generality. The same consideration can be made for the incoming light, which is all concentrated in the portion $dE(\mathcal{M},\mathbf{i})$ of irradiance reaches $\mathcal{M}$, leading to $dE(\mathcal{M},\mathbf{i}) \rightarrow E(\mathcal{M},\mathbf{i})$. Thus, using Equation 2, this quantity is expressed as the product of the BSDF and the irradiance from the direction $\mathbf{i}$:

$$L_o(\mathcal{M},\mathbf{o}) = f(\mathcal{M},\mathbf{i},\mathbf{o})\ E(\mathcal{M},\mathbf{i}). \tag{3}$$

Depending on the sensor configuration (Section C), the space of outgoing directions Ω is divided into cells, each covering a subspace of outgoing directions $\Omega_\mathbf{o}$, centered around direction $\mathbf{o}$ (Figure 1-[c-d]). The complete hemisphere thus gathers all the radiance samples reflected by $\mathcal{M}$ for all possible outgoing directions $\mathbf{o}_j \in \Omega_\mathbf{o}$. In other words, each cell of the sensor stores a portion of the reflected radiant exitance M_e:

$$\Delta M_e(\mathcal{M},\mathbf{o}) = \int_{\Omega_\mathbf{o}} L_o(\mathcal{M},\mathbf{o}_j)\cos\theta_{\mathbf{o}_j}\, d\omega_{\mathbf{o}_j}. \tag{4}$$

One sensor cell gathers the mean value of all the collected radiance samples reflected by $\mathcal{M}$ i.e. the mean of the integrand in Equation 4:

$$\begin{aligned}\frac{\Delta M_e(\mathcal{M},\mathbf{o})}{\Omega_\mathbf{o}} &= \frac{\int_{\Omega_\mathbf{o}} L_o(\mathcal{M},\mathbf{o}_j)\cos\theta_{\mathbf{o}_j}\, d\omega_{\mathbf{o}_j}}{\Omega_\mathbf{o}} \\ &= \overline{L_o(\mathcal{M},\mathbf{o})\cos\theta_o} \\ &= E(\mathcal{M},\mathbf{i})\ \overline{f(\mathcal{M},\mathbf{i},\mathbf{o})\cos\theta_o}.\end{aligned} \tag{5}$$

Finally,

$$\overline{f(\mathcal{M},\mathbf{i},\mathbf{o})\cos\theta_o} = \frac{\int_{\Omega_\mathbf{o}} L_o(\mathcal{M},\mathbf{o}_j)\cos\theta_{\mathbf{o}_j}\, d\omega_{\mathbf{o}_j}}{\Omega_\mathbf{o}\ E(\mathcal{M},\mathbf{i})} \tag{6}$$

with:

$$\lim_{\Omega_\mathbf{o}\to 0} \frac{\int_{\Omega_\mathbf{o}} L_o(\mathcal{M},\mathbf{o}_j)\cos\theta_{\mathbf{o}_j}\, d\omega_{\mathbf{o}_j}}{\Omega_\mathbf{o}\ E(\mathcal{M},\mathbf{i})} = f(\mathcal{M},\mathbf{i},\mathbf{o})\cos\theta_o. \tag{7}$$

This last relation shows that thinner cells tend to represent more accurately BSDF values (Section C). The resulting histogram (i.e., values associated with each sensor's cell) is proportional to $f(\mathcal{M},\mathbf{i},\mathbf{o})\cos\theta_o$, with $\mathbf{o}$ the center direction of one sensor's cell. This cosine weighted BSDF typically corresponds to the measurement produced by an actual gonioradiometer [43].

The integral in Equation 6 cannot be analytically evaluated, but its integral form is closely related to the *Light Transport Equation* [44, 45], often managed using path tracing techniques. When an incoming direction $\mathbf{i}$ is fixed, a complete light path is randomly built until it leaves the material, from above in case of reflection and below for refraction. Energy that leaves the sample from the sides is considered as *invalid*, and the corresponding light path is gathered by side sensors as explained in Section C.2. Depending on the outgoing direction $\mathbf{o}_j$, the light path contribution is accumulated on the corresponding sensor's cell. Using the definition of radiance,

$$L_o(\mathcal{M},\mathbf{o}_j) = \frac{d^2\Phi(\mathcal{M},\mathbf{o}_j)}{\cos\theta_{\mathbf{o}_j}\, d\omega_{\mathbf{o}_j}\, dA}, \tag{8}$$

Equation 4 can be written as

$$\int_{\Omega_\mathbf{o}} \frac{d^2\Phi(\mathcal{M},\mathbf{o}_j)}{\cos\theta_{\mathbf{o}_j}\, d\omega_{\mathbf{o}_j}\, dA}\cos\theta_{\mathbf{o}_j}\, d\mathbf{o}_j \approx \sum_{j=1}^{k} \frac{\Phi_j(\mathcal{M},\mathbf{o}_j)}{A_\mathcal{M}}, \tag{9}$$

where the approximation corresponds to a density estimation of the propagated flux by the k rays leaving $\mathcal{M}$ (with projected area $A_\mathcal{M}$) and reaching the corresponding cell after one or multiple bounces on $\mathcal{M}$. Each light ray is initialized with a portion of the input flux Φ_p (in our case $\Phi_p = \frac{\Phi_e}{N} = \frac{1}{N}$, where N is the total number of light rays shot on the material and Φ_e the input flux of our collimated beam received by the projected area $A_\mathcal{M}$) modulated by facets BSDF through multiple bounces along the path propagation on $\mathcal{M}$. Finally, each cell gathers a quantity of light energy that depends on the number of captured light paths:

$$f(\mathcal{M},\mathbf{i},\mathbf{o})\cos\theta_o \approx \frac{\sum_{j=1}^{k}\Phi_j(\mathcal{M},\mathbf{o}_j)}{\Omega_o\ E(\mathcal{M},\mathbf{i})\ A_\mathcal{M}}. \tag{10}$$

This last Equation also corresponds to a density estimation on the space of directions, calculated over a solid angle Ω_o. The light path simulation process is similar to the one described in [46]. However ray sampling requires attention in order to manage intersections with the first interface. Our system proceeds as follows (see Figure 3): (i) Sample a point p on the middle plane of the interface; (ii) From p and direction $\mathbf{i}$, a point o is computed as the intersection between the bounding box of this interface; (iii) Finally, the initial ray of the light path starts from this intersection point o in direction $\mathbf{d} = -\mathbf{i}$. Our initialization process guarantees a uniform sampling of the macro-surface (and actually corresponds to the projected area $A_\mathcal{M}$ of the material patch).

C. Virtual Sensor

The gonioradiometer configuration we propose is built upon two distinct types of sensors: hemispherical sensors (Section C.1) and spatial sensors (Section C.2). Valid light paths (Figure 1-[b-1]) denoted as L_1 and L_{2+}, are captured by the upper hemispherical sensor. Invalid light paths, leaving the sample by the four sides, are gathered by a set of four hemispherical sensors associated with four planar sensors. Their goal is to collect both directional and spatial distributions.

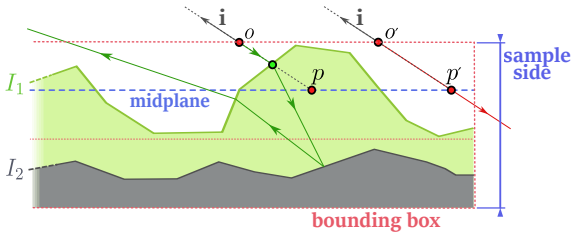

Fig. 3. Ray sampling initialization process: a point p is uniformly sampled on the midplane of the first interface, and projected onto the axis-aligned bounding box using direction $\mathbf{i}$ to obtain a ray origin o. When the ray misses the interface (p' shows the failure case), the sample is discarded.

C.1. Hemispherical sensor for BSDF and distribution of energy loss

In order to ensure sensor cells with regular shapes and uniform distribution on the hemisphere, the subdivision scheme has to be carefully chosen. Figure 4 shows two examples of subdivisions. The first one uses a simple zenithal and azimuthal scheme, providing undesired shape variations of the produced cells; the second one corresponds to an igloo subdivision scheme with better shape and distribution properties. Beckers et al. [39] propose a method to divide a hemisphere into cells of constant size. According to this paper, we propose to define the hemisphere cap with a given angle θ_0^f as the first cell; the next ones are constructed according to:

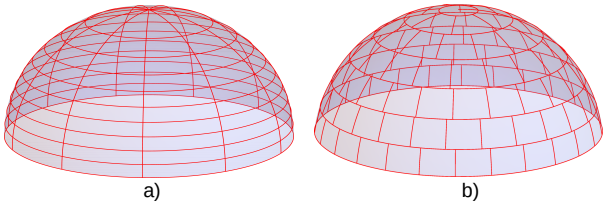

Fig. 4. Two hemispherical sensors with approximately the same number of cell: a) 110 cells with a simple height and azimuthal subdivision, cells have all the same area; b) 112 cells with igloo subdivision.

$$
\begin{aligned}
&1) \quad \theta_{j+1}^f = \theta_j^f + 2 \times \sin\left(\frac{\theta_j^f}{2}\right) \times \sqrt{\frac{\pi}{k_j}} \\
&2) \quad r_{j+1} = 2 \times \sin\left(\frac{\theta_{j+1}^f}{2}\right) \\
&3) \quad k_{j+1} = \lfloor k_j \left(\frac{r_{j+1}}{r_j}\right)^2 \rceil \\
&4) \quad \theta_{j+1}^f = \cos^{-1}\left(\cos\left(\theta_j^f\right) - (k_{j+1} - k_j)(1 - \cos\left(\theta_0^f\right)\right)
\end{aligned}
\tag{11}
$$

where r_j, k_j and θ_j^f are respectively the radius, the number of cells and the zenital angle of ring j. $\lfloor x \rceil$ represents the rounding value of x. The cell size is manually adjusted with θ_0^f so as to guarantee that the last row θ_j^f is aligned with $\frac{\pi}{2}$.

Each cell of the hemisphere is a sensor that collects all measured values over the area dA from the lighting simulation process, as a real photodetector. It stores all the gathered samples in a stack and the final BSDF value is calculated as the mean (or median) value. As for a real photometric sensor and because the final value is generally associated to the center coordinates of a cell, a bias corresponding to θ and φ for each measured value (Figure 1-d) may have to be managed. The accuracy of a virtual BRDF measurement therefore depends on the size of its cells.

In order to capture the directional distribution of the energy lost through the sample sides between two successive layers, our system also deploys hemispherical sensors associated with the (vertical) borders of the sample. With a square shaped sample, four hemispherical samples are thus required for the four sides (Figure 5-b).

C.2. Sensor for spatial distribution of energy loss

Spatial distribution of the energy lost between two layers through sample sides is also interesting to capture and analyze. We propose to place planar sensors parallel to the sample sides, so as to surround its bounding box. Each plane is associated with a regular grid of pixels, as illustrated in Figure 5-a. Each pixel gathers the radiant exitance. Because the spatial sensor rectangle surrounds the sample side, some pixels, located above the upper interface do not capture any light energy (it will be received by the main BSDF sensor).

3. APPLICATION CASES AND RESULTS

We propose to evaluate the efficiency and the modularity of our virtual gonioradiometer through different layered material configurations. The ray tracing process employed relies on the Embree kernel library [47].

I_n	n^{th} interface.
σ_n	Roughness of n^{th} interface (In our case, it is the standard deviation of a Beckmann Normal Distribution Function.
η_n	Refractive index of n^{th} medium.
θ_i	Angle between incident light and interface normal.
h_n	Thickness (mm) between I_n and I_{n+1}.
Φ_1,Φ_{2+}	Radiant flux (W) captured from single scattering and multiple (excluding the first) scattering
L_1,L_{2+}	Radiance ($\text{W} \cdot \text{m}^{-2} \cdot \text{sr}^{-1}$) captured from single scattering and multiple (excluding the first) scattering.
Φ_{XZ0},Φ_{XZ1}, Φ_{YZ0},Φ_{YZ1}	Radiant flux (W) captured from the four boundaries of the material sample (Figure 5).
E_{XZ0},E_{XZ1}, E_{YZ0},E_{YZ1}	Radiant exitance ($\text{W} \cdot \text{m}^{-2}$) captured from the four boundaries.
L_{XZ0},L_{XZ1}, L_{YZ0},L_{YZ1}	Radiance ($\text{W} \cdot \text{m}^{-2} \cdot \text{sr}^{-1}$) captured from the four boundaries.

Table 1. Notations used in the results section.

Table 1 provides the notations employed in the following. Interfaces between layers are defined by triangular meshes, produced from a Beckmann normal distribution function with a pre-determined value of σ, with the process described by Ribardiere et al. [40]. For the sake of clarity, all the results have been produced with materials corresponding to isotropic distributions of microfacets, but the general process presented in this paper can be applied for any type of surfaces.

We also propose to employ two strategies for avoiding side energy loss and simulate infinite samples. They are usually

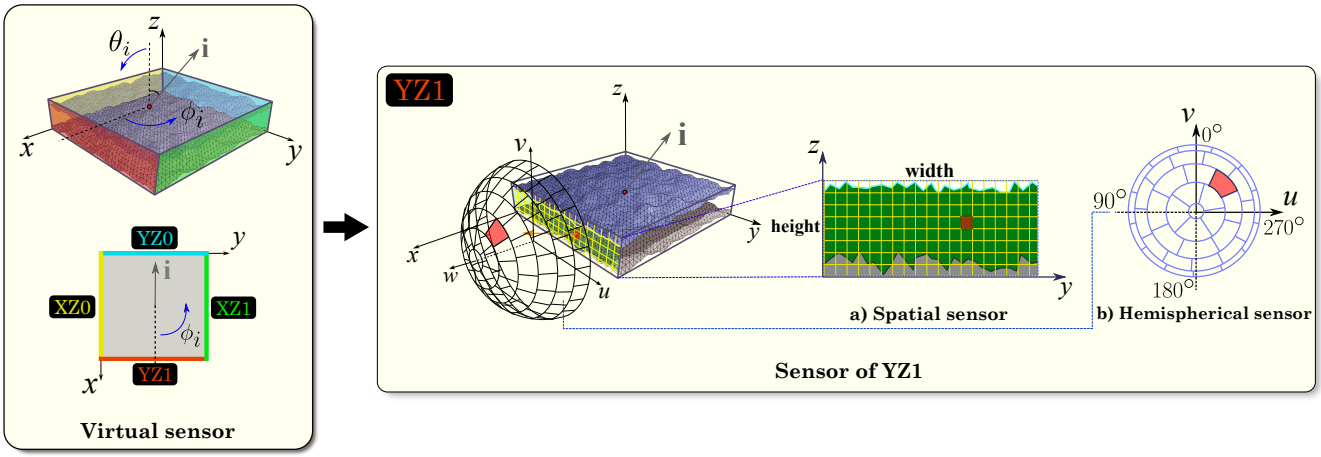

Fig. 5. Sensor design for capturing and quantifying the energy lost through the sample sides (red, green, blue and yellow regions on the left figure). One planar and one hemispherical sensor are aligned with each side. Couples of sensors are denoted as XZ0, XZ1, YZ0, and YZ1 respectively. a) Spatial sensors are used to capture the spatial distribution of the energy. b) Illustration of the hemispherical sensor employed for side XZ1 (red side). In Section 3, directional distributions correspond to projections based on each local coordinates frame u, v, w.

employed in lighting simulation systems or as initial assumption to derive statistical layered BSDF model [16, 17].

- Position-free: related with the microfacet theory, the goal is to consider that light may propagate from any point on the (statistical) surface, neglecting thickness between two layers. It consists in randomly repositioning the intersection between the incoming ray and the next interface in the light path (Figure 6-a).
- Mirror-tiling: the surface mesh is virtually extended infinitely using a mirror replication scheme, the ray is thus propagated from a new origin in the same sample, (Figure 6-b);

These two strategies re-integrate light rays that would leave the sample by one side in the volume at a new origin, in order to continue propagation. This process thus ensures energy conservation. Only a subset of configurations we used to conduct our study are provided in the article; We encourage readers to read the supplemental material for more detailed and general results.

A. Analysis of results

This section proposes an analysis of simulated appearances that correspond to multi-layered materials, with varying thicknesses and optical properties. We specifically focus on the energy transmitted by the sample sides and its distribution in space and direction. We briefly show that our system can be naturally generalized to higher number of layers for this analysis of edge energy loss, we provide an example with three layers.

In order to ensure the correctness of our simulation process, we have made comparisons with analytical representations that corresponds to a single layer, set with a mirror material. Figure 7 illustrates two cases, showing that simulations can be noisy with rough surfaces, but the implemented process actually provides the expected values.

A.1. Thickness layer variation

Table 2 presents the energy distribution obtained for a perpendicular incident direction $\theta_i = 0°$ on a two-layer material, defined by a slightly rough water layer ($\sigma_1 = 0.05$) atop a perfectly flat diffuse substrate. Φ_1 corresponds to the first reflection, it

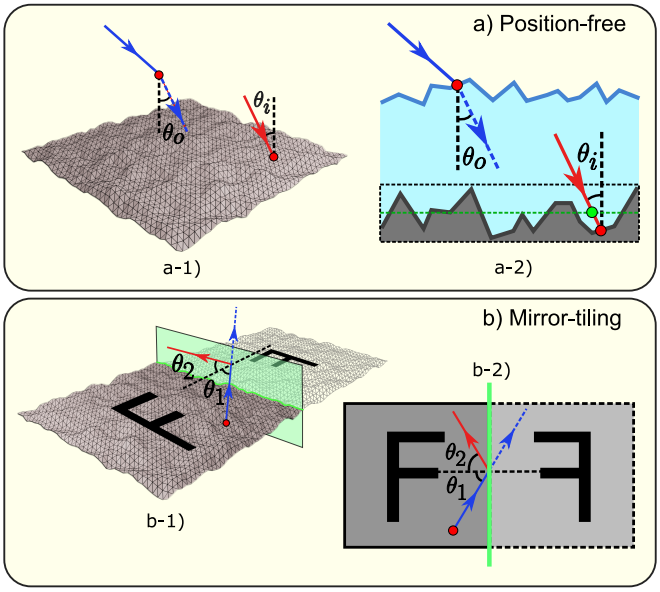

Fig. 6. Path tracing without loss of energy. The blue ray corresponds an incident direction; the red ray illustrates the propagation scheme. a) Position-free approach, each incident direction leads to a repositioning: red points are actual ray-interface intersections, the green point is randomly selected on the middle plane of surface bounding box for randomly repositioning the light path, $\theta_o = \theta_i$. b) Mirror-tiling approach, $\theta_1 = \theta_2$, where F represents the actual interface mesh, the ray is propagated according to a virtual mirror representation. b-1) 3D view; b-2) top-view.

remains unchanged independently of the chosen simulation strategy. Given that our defined material does not absorb any energy, $\Phi_1 + \Phi_{2+}$ should be equal to 1. The number of invalid light paths increases accordingly with layers thickness h_1 (Figure 8).

Another interesting observation from Figure 8 is the pro-

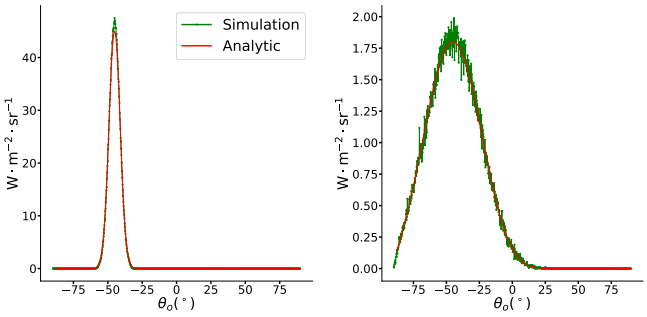

(a) (b)

Fig. 7. Distribution of L_1 (1D slice at $\phi = 0°$) in using Beckmann Normal Distribution Function with $\theta_i = 45°$. Configuration settings: (a) $\sigma = 0.05$, (b) $\sigma = 0.25$.

nounced impulse at $\theta_i = 0°$, which corresponds to the direction of incidence (see Figure 9). This phenomenon is more visible with low thickness values h_1. It appears because of the high probability that a ray reflected by the substrate leaves and passes through the same input facet again (the solid angle associated with the top microfacet is high), with a statistically very close outgoing direction. This impulse decreases as thickness increases (because the solid angle associated with the top microfacet decreases as well). This phenomenon is not present with the "position free" scheme (Figure 8-b), because input and output microfacets become uncorrelated.

Φ_1	Φ_{2+}			
	Position-free	h_1 (mm)	Mirror-tiling	w/o Side Energy
0.020	0.980	0.05	0.980	0.916
		0.2	0.980	0.768
		2	0.979	0.337

Table 2. Total flux reflected by a two-layer material, defined by $\sigma_1 = 0.05$, $\sigma_2 = 0$, $\eta_1 =$ Air, $\eta_2 =$ Water, and a flat Lambertian substrate with $\rho = 1$, $\theta_i = 0°$. Φ_{2+} varies according to thickness h_1. Our system naturally handles several simulation methods, including position-free and mirror-tiling.

A.2. Energy loss through sample sides

σ_1	Φ_1	Φ_{2+}	Φ_{XZ0}	Φ_{XZ1}	Φ_{YZ0}	Φ_{YZ1}
0.05	0.028	0.244	0.114	0.114	0.433	0.066
0.15	0.029	0.239	0.117	0.117	0.432	0.066
0.25	0.031	0.230	0.119	0.119	0.435	0.066

Table 3. Captured radiant flux for a two-layer material, configuration settings: $\sigma_2 = 0$, $\eta_1 =$Air, $\eta_2 =$Water, diffuse($\rho = 1$) as substate BSDF material, $\theta_i = 45°$, $h_1 = 2$mm.

This section discusses the results obtained with a light incident angle $\theta_i = 45°$, a material composed of two layers (rough water at the top) with a top layer thickness equal to $h_1 = 2\mu$m and the top interface roughness set to σ_{I_1}. Table 3 provides the total captured radiant flux. The YZ0 sensor (positioned on the opposite side of the incident direction) records the highest energy, and Figure 10 provides the distributions of L_1 and L_{2+}. An increase in the water surface layer's roughness appears to even the distribution of L_1 out. Considering the directional sensor data YZ0 in Figure 11 (parallel to the incident plane), a pronounced energy peak appears around $\theta = 90°$ and $\phi = 145°$. It corresponds to rays refracted by the water surface and directly captured by the sensor. It becomes wider as the top water interface roughness increases because the transmission lobe in the water layer spreads. In addition, the energy lost by the sides increases according to roughness, even though the substrate is flat and Lambertian, because the transmitted flux spreads when the interface roughness increases. The spatial sensor values are also more noisy as the interface roughness increase, due to the spreading of reflected light directions.

A.3. Substrate material variation

σ_2	Substrate BSDF	Φ_1	Φ_{2+}	Φ_{XZ0}	Φ_{XZ1}	Φ_{YZ0}	Φ_{YZ1}
0.15	Perfect mirror	0.028	0.314	0.024	0.023	0.611	0.0
0.25	Perfect mirror		0.288	0.039	0.039	0.606	0.0
0.00	Diffuse ($\rho = 1$)		0.244	0.114	0.114	0.433	0.066

Table 4. Two-layer material, configuration settings: $\sigma_1 = 0.05$, η_1=Air, η_2=Water, $\theta_i = 45°$, $h_1 = 2$mm, the remaining configurations are noted in the table. The variation in the Radiant flux captured Φ_1, Φ_2 and lost radiant flux Φ_{XZ0}, Φ_{XZ1}, Φ_{YZ0}, Φ_{YZ1}.

Fixing the roughness value σ_1, we propose to study the effect of varying the substrate material and its roughness σ_2, in order to assess the shift from slightly glossy to fully diffuse surfaces. The total radiant flux captured by each sensor is provided in Table 4. Notably, according to the substrate roughness, the radiant flux captured by sensor YZ0 decreases. It is balanced by an increase of radiant flux on the other boundary sensors, consistent with energy conservation principles. Φ_{YZ1} (aligned with the incident direction) registers a nonzero value once the substrate is completely diffuse. The distribution of L_1 and L_{2+} is illustrated in Figure 12. The L_1 distribution remains constant due to the unchanged water surface configuration. Conversely, as the substrate's glossiness decreases, the distribution of L_{2+} becomes more uniform. The supplemental material illustrates many configurations that result in variations of distributions captured by the sensors.

A.4. Tri-layered material

We also explored reflected light distribution with 3 layers, under various angles of incidence. Table 5 provides the general reflected flux. Consistently with Fresnel law, an increase in the angle of incidence θ_i leads to a higher Φ_1. Consequently, a greater proportion of radiant flux is captured by sensor YZ0 (positioned on the opposite side of the incident direction), compared with other boundary sensors. Distributions of L_1 and L_{2+} are depicted in Figure 13. A back-reflection impulse also appears, again due to the low thickness values ($h_1 = h_2 = 0.2$mm). With $\theta_i = 80°$, the impulse in L_{2+} is indicative of multi-scattering within the singular water surface layer, emphasizing that multi-scattering becomes non-negligible as the incident angle increases. The radiance distribution for sensor YZ0 is detailed in Figure 14, where the two impulses are due to refractions from both the water and pyrex surfaces. Given the diffuse material of the substrate, the spatial distribution of radiant exitance between layers is relatively uniform.

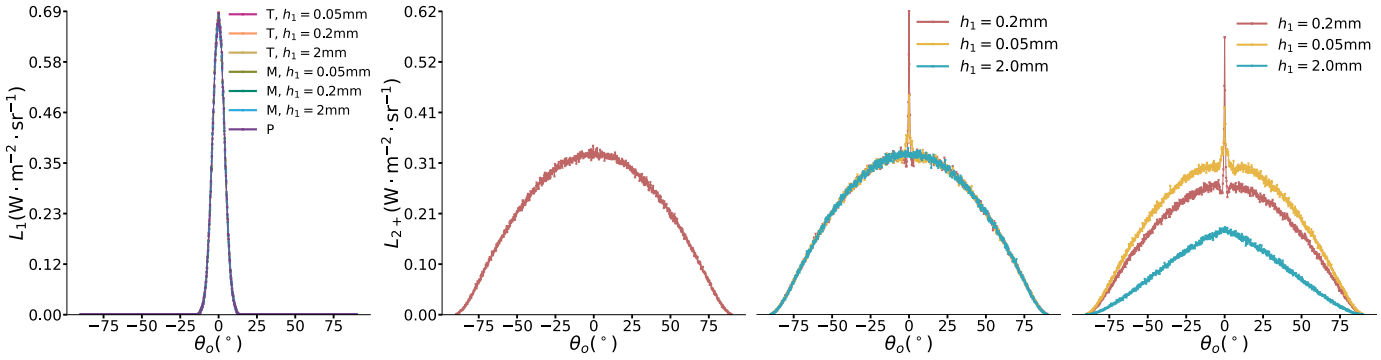

(a) L_1 (b) Position-free (c) Mirror-tiling (d) w/o Side Energy

Fig. 8. Distribution of radiance L_1 and L_{2+}, captured by the sensor corresponding to values presented in Table 2, with $\phi = 0°$. All interfaces are isotropic, 2D slices in the incident plane are representative of the BRDF. (a) L_1 distribution, P: Position free, T: Tiling and M: Measurement; (b) distribution of L_{2+} with the position-free scheme; (c) distribution of L_{2+} with the position-free scheme; (d) distribution of L_{2+} without side energy loss.

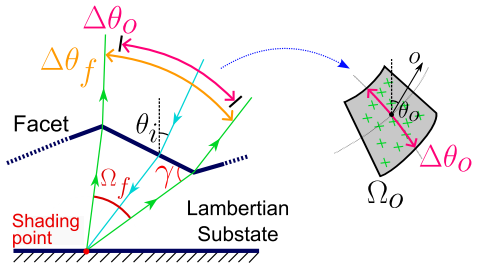

Fig. 9. Back-reflection impulse. Ω_f: angle solid of facet at shading point. $\Delta\theta_f$: the range of angle θ between reflect ray that pass through the input facet and the surface normal. Ω_o: the solid angle of sensor cell. $\Delta\theta_o$: the range of angle θ of sensor cell.

$\theta_i(^\circ)$	Φ_1	Φ_{2+}	Φ_{XZ0}	Φ_{XZ1}	Φ_{YZ0}	Φ_{YZ1}
15	0.02	0.599	0.093	0.093	0.111	0.085
45	0.028	0.576	0.089	0.089	0.148	0.070
80	0.340	0.376	0.059	0.058	0.128	0.040

Table 5. Tri-layer material scattering. Configuration settings: $\sigma_1 = 0.05$, $\sigma_2 = 0.05$, $\sigma_3 = 0$, η_1 =Air, η_2 =Water, η_3 =Pyrex, diffuse ($\rho = 1$). Substrate BSDF material: $h_1 = 0.2$mm, $h_2 = 0.2$mm. Variation in radiant flux is given by Φ_1, Φ_2, and lost radiant flux is given by Φ_{XZ0}, Φ_{XZ1}, Φ_{YZ0}, Φ_{YZ1}.

B. Limitations

The light energy spread by the sample sides can be measured by our virtual system, but devising an analytical model is not straightforward. It would be interesting to further study these effects in order to propose approximations that could depend on the material parameters (i.e. layer thickness, optical properties, etc.). Using participating media in the simulation process would also be a very appealing option for representing and analyzing more complex materials. As long as the layers interface is defined by a mesh geometry and the layer material may be managed with ray tracing techniques (even in the case of participating media, and/or microflakes distributions, for instance defined by small disks), our goniophotometer should be able

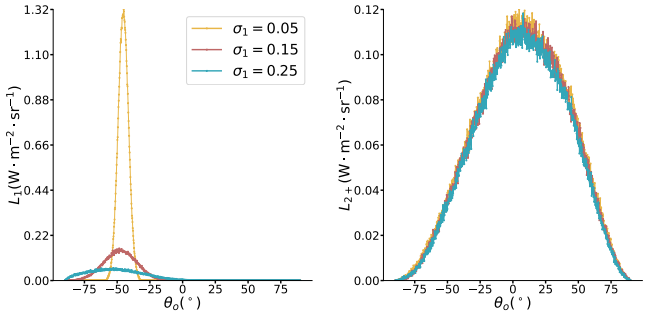

(a) (b)

Fig. 10. Distribution of L_1 and L_{2+} (1D slice of sensor data at $\phi = 0°$) in Table 3.

to capture reflected and transmitted light distributions. However, thin effects produced by sparkles might be smoothed by the sensor resolution. For specific high frequencies, different sensor configurations could or should be managed, either using a hierarchical sensor representation [34] as shown for instance by [48] with a real gonioradiometer capable of handling very high resolutions in specific outgoing directions.

4. CONCLUSION

This paper proposes a complete framework for virtually capturing the light scattered by layered materials. The opaque substrate can be represented by a flat Lambertian surface or a rough conductor, and layers' thickness can be controlled by the user. Light scattering is simulated using a ray tracing approach, and several sensors capture the spatial and directional distributions. Our system can be employed for understanding side effects that result in energy loss when considering reflectance only. We have also integrated two types of simulation schemes (point-free and mirror-tiling) for representing infinite samples.

We propose several materials configurations, in order to demonstrate the effectiveness and the scalability of our system. The obtained results illustrate the distribution of the direct reflection (L_1) as well as the reflection that comes from multiple scattering in the medium (L_{2+}). Light energy lost in the layer's

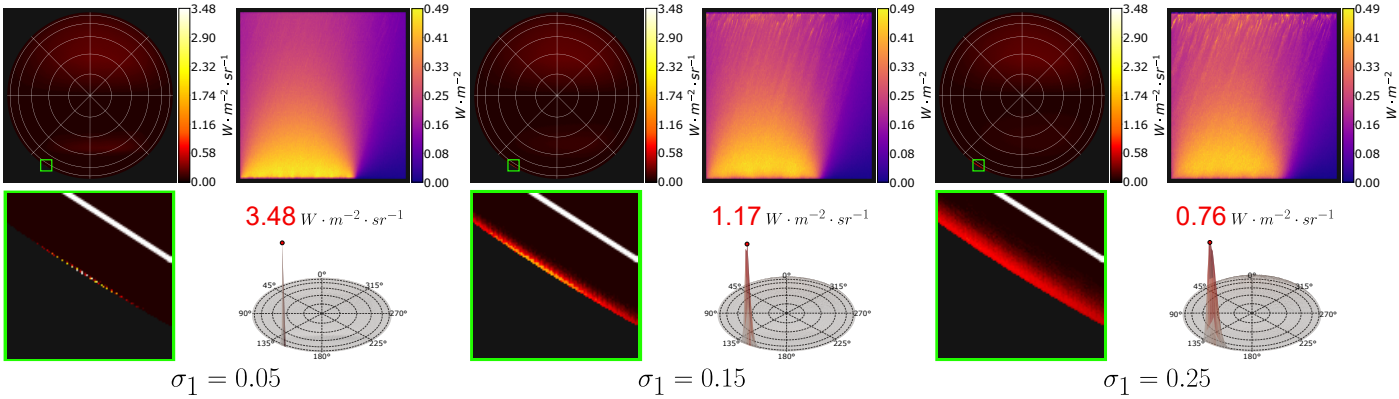

Fig. 11. Energy loss captured by sensor XZ0 for 3 configurations. For each, (top-left) is the directional distribution of L_{XZ0}, (top-right) the spatial distribution of E_{XZ0}, (bottom-left) shows in detail the peak in directional distribution (surrounded by a green box) and (bottom-right) a 3D representation of the directional distribution of the radiance.

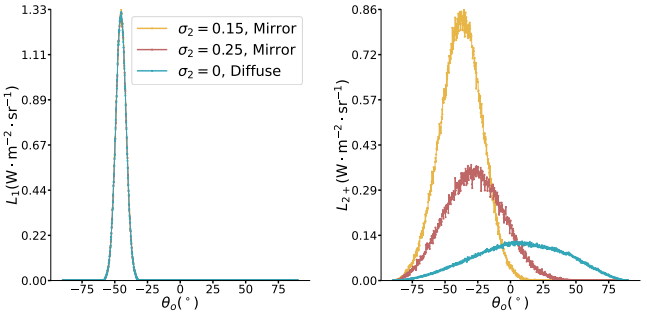

(a) (b)

Fig. 12. Distribution of L_1 and L_{2+} (1D slice of sensor data at $\phi = 0°$) in Table 4.

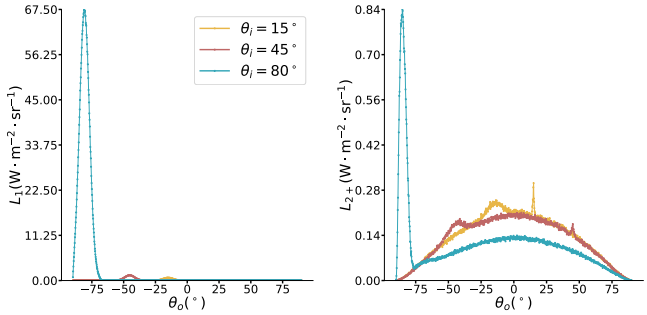

(a) (b)

Fig. 13. Distribution of L_1 and L_{2+} (1D slice of sensor data at $\phi = 0°$) in Table 5.

sides varies according to the water layer thickness, the substrate roughness and the choice of its reflectance. We also provide plots of the angular distribution of the reflection that can be employed for the analysis of the global aspect of such surfaces.

Several interesting questions can be addressed in the future. This framework can be a basis for designing and controlling the appearance of complex materials for industrial applications. Its extension for better understanding multi-resolution appearance would be an interesting challenge, in order to manage multi-layered surfaces with several levels of detail.

ACKNOWLEDGEMENT

This research was funded, in whole or in part, by the French National Research Agency (ANR) under the REFLECTIVITY project : ANR-22-CE22-0006.

DISCLOSURES

The authors declare no conflicts of interest.

REFERENCES

1. M. Oren and S. K. Nayar, "Generalization of lambert's reflectance model," in ACM SIGGRAPH proceedings, (1994).
2. B. Walter, S. R. Marschner, H. Li, and K. E. Torrance, "Microfacet models for refraction through rough surfaces," in Computer Graphics Forum, EGSR proceedings, (2007).
3. K. E. Torrance and E. M. Sparrow, "Theory for off-specular reflection from roughened surfaces," J. Opt. Soc. Am. **57** (1967).
4. R. L. Cook and K. E. Torrance, "A reflectance model for computer graphics," in ACM SIGGRAPH proceedings, (1982).
5. C. Bourlier, G. Berginc, and J. Saillard, "One- and two-dimensional shadowing functions for any height and slope stationary uncorrelated surface in the monostatic and bistatic configurations," IEEE Transactions on Antennas Propag. **50** (2002).
6. M. Ashikhmin, S. Premoze, and P. Shirley, "A microfacet-based BRDF generator," in Proceedings of the 27th Annual Conference on Computer Graphics and Interactive Techniques, SIGGRAPH 2000, New Orleans, LA, USA, July 23-28, 2000, (ACM, 2000), pp. 65–74.
7. C. Kelemen and L. Szirmay-Kalos, "A Microfacet Based Coupled Specular-Matte BRDF Model with Importance Sampling," in Eurographics 2001 - Short Presentations, (Eurographics Association, 2001).
8. M. M. Bagher, C. Soler, and N. Holzschuch, "Accurate fitting of measured reflectances using a shifted gamma micro-facet distribution," Comput. Graph. Forum **31** (2012).
9. J. Dupuy, E. Heitz, J. Iehl, P. Poulin, F. Neyret, and V. Ostromoukhov, "Linear efficient antialiased displacement and reflectance mapping," ACM Trans. Graph. **32**, 211:1–211:11 (2013).
10. M. Ribardière, B. Bringier, D. Meneveaux, and L. Simonot, "STD: Student's t-Distribution of Slopes for Microfacet Based BSDFs," Comput. Graph. Forum (2017).
11. E. Heitz, "Understanding the masking-shadowing function in microfacet-based brdfs," J. Comput. Graph. Tech. **3** (2014).
12. B. Smith, "Geometrical shadowing of a random rough surface," IEEE Transactions on Antennas Propag. **15**, 668–671 (1967).

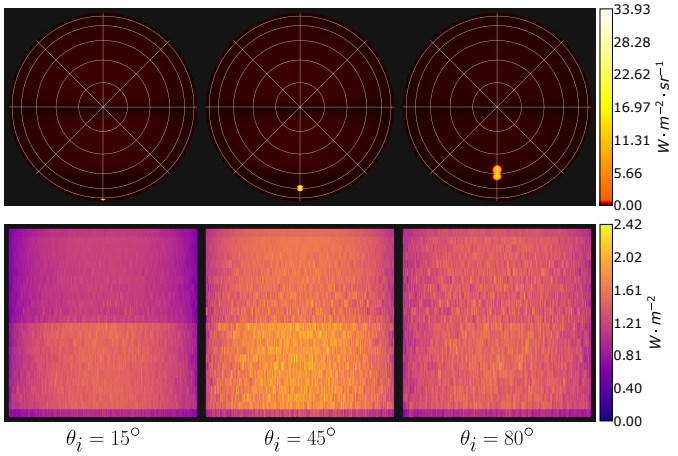

Fig. 14. Directional distribution of L_{YZ0} and spatial distribution of E_{YZ0} exhibit two impulses due to refraction on the middle interface in tri-layered material (Table 5).

13. E. Heitz, J. Hanika, E. d'Eon, and C. Dachsbacher, "Multiple-scattering microfacet bsdfs with the smith model," ACM Trans. Graph. **35**, 58:1–58:14 (2016).
14. Q. Zhu, H. Lee, and Z. M. Zhang, "Radiative properties of materials with surface scattering or volume scattering: A review," Front. Energy Power Eng. China **3**, 60–79 (2009).
15. D. Meneveaux, B. Bringier, E. Tauzia, M. Ribardiere, and L. Simonot, "Rendering rough opaque materials with interfaced lambertian microfacets," IEEE Transactions on Vis. Comput. Graph. **24**, 1368–1380 (2018).
16. L. Belcour, "Efficient Rendering of Layered Materials using an Atomic Decomposition with Statistical Operators," ACM Transactions on Graphics **37**, 1 (2018).
17. Y. Guo, M. Hašan, and S. Zhao, "Position-free monte carlo simulation for arbitrary layered bsdfs," ACM Trans. Graph. **37** (2018).
18. J. Randrianandrasana, P. Callet, and L. Lucas, "Transfer matrix based layered materials rendering," ACM Transactions on Graphics **40**, Article No. 177, 16 p (2021).
19. H. de Dinechin and L. Belcour, "Rendering layered materials with diffuse interfaces," Proc. ACM Comput. Graph. Interact. Tech. **5** (2022).
20. B. Wang, W. Jin, M. Hašan, and L.-Q. Yan, "Spongecake: A layered microflake surface appearance model," ACM Trans. Graph. **42** (2022).
21. C. Wang, A. Wilkie, P. Harcuba, and L. Novosad, "Virtual ellipsometry on layered micro-facet surfaces," Opt. Express **25**, 22971–22990 (2017).
22. V. Falster, A. Jarabo, and J. R. Frisvad, "Computing the bidirectional scattering of a microstructure using scalar diffraction theory and path tracing," in Computer Graphics Forum, vol. 39 (Wiley Online Library, 2020), pp. 231–242.
23. H. Wu, J. Dorsey, and H. Rushmeier, "Physically-based interactive bi-scale material design," ACM Transactions on Graph. (TOG) **30**, 1–10 (2011).
24. B. Cabral, N. Max, and R. Springmeyer, "Bidirectional reflection functions from surface bump maps," SIGGRAPH Comput. Graph. **21**, 273–281 (1987).
25. S. H. Westin, J. R. Arvo, and K. E. Torrance, "Predicting reflectance functions from complex surfaces," SIGGRAPH Comput. Graph. **26**, 255–264 (1992).
26. A. Krishnaswamy, G. V. G. Baranoski, and J. G. Rokne, "Virtual goniophotometric measurements protocol," Tech. Rep. CS-2002-21, School of Computer Science, University of Waterloo (2002).
27. T. Wong, L. Wan, C. Leung, and P. Lam, "Real-time environment mapping with equal solid-angle spherical quad-map," Shader X4: Light. & Render. (2006).
28. L. Wan, T. Wong, and C. Leung, "Isocube: Exploiting the cubemap hardware," IEEE Trans. Vis. Comput. Graph. **13**, 720–731 (2007).
29. P. Leopardi, "A partition of the unit sphere into regions of equal area and small diameter." ETNA. Electron. Transactions on Numer. Analysis [electronic only] **25**, 309–327 (2006).
30. P. Tregenza, "Subdivision of the sky hemisphere for luminance measurements," Light. Res. & Technol. **19**, 13–14 (1987).
31. K. M. Gorski, E. Hivon, A. J. Banday, B. D. Wandelt, F. K. Hansen, M. Reinecke, and M. Bartelmann, "HEALPix: A framework for high-resolution discretization and fast analysis of data distributed on the sphere," The Astrophys. J. **622**, 759–771 (2005).
32. J. F. Blinn, "Simulation of wrinkled surfaces," SIGGRAPH Comput. Graph. **12**, 286–292 (1978).
33. B. Bringier, M. Ribardière, D. Meneveaux, and L. Simonot, "Design of rough microgeometries for numerical simulation of material appearance," Appl. Opt. **59**, 4856–4864 (2020).
34. J. S. Gondek, G. W. Meyer, and J. G. Newman, "Wavelength dependent reflectance functions," in Proceedings of the 21st Annual Conference on Computer Graphics and Interactive Techniques, (Association for Computing Machinery, New York, NY, USA, 1994), SIGGRAPH '94, p. 213–220.
35. W. Jakob, E. d'Eon, O. Jakob, and S. Marschner, "A comprehensive framework for rendering layered materials," ACM Trans. Graph. **33** (2014).
36. W. Jakob, "layerlab: A computational toolbox for layered materials," in SIGGRAPH 2015 Courses, (ACM, New York, NY, USA, 2015), SIGGRAPH '15.
37. T. Zeltner and W. Jakob, "The layer laboratory: A calculus for additive and subtractive composition of anisotropic surface reflectance," Transactions on Graph. (Proceedings SIGGRAPH) **37**, 74:1–74:14 (2018).
38. M. Bati, R. Pacanowski, and P. Barla, "Comparative study of layered material models," in Workshop on Material Appearance Modeling, H. Rushmeier and R. Klein, eds. (Strasbourg, France, 2019).
39. B. Beckers and P. Beckers, "A general rule for disk and hemisphere partition into equal-area cells," Comput. Geom. **45**, 275–283 (2012).
40. M. Ribardière, B. Bringier, L. Simonot, and D. Meneveaux, "Microfacet bsdfs generated from ndfs and explicit microgeometry," ACM Trans. Graph. **38** (2019).
41. F. Pérez-Ràfols and A. Almqvist, "Generating randomly rough surfaces with given height probability distribution and power spectrum," Tribol. Int. **131**, 591–604 (2019).
42. N. Prouteau, C. Joubert, B. Bringier, and M. Khoudeir, "Continuous material reflectance map for deep photometric stereo," JOSA A **40**, 792–802 (2023).
43. J. Dupuy and W. Jakob, "An adaptive parameterization for efficient material acquisition and rendering," Transactions on Graph. (Proceedings SIGGRAPH Asia) **37**, 274:1–274:18 (2018).
44. E. Veach, "Robust Monte Carlo Methods for Light Transport Simulation," Ph.D. thesis, Stanford University (1997).
45. M. Pharr, W. Jakob, and G. Humphreys, Physically Based Rendering: From Theory to Implementation (3rd ed.) (Morgan Kaufmann Publishers Inc., San Francisco, CA, USA, 2016), 3rd ed.
46. M. Pharr, W. Jakob, and G. Humphreys, Physically based rendering: From theory to implementation (MIT Press, 2023), chap. 13.2.
47. I. Wald, S. Woop, C. Benthin, G. S. Johnson, and M. Ernst, "Embree: A kernel framework for efficient cpu ray tracing," ACM Trans. Graph. **33** (2014).
48. G. Obein, O. Shiraz, and G. Ged, "Evaluation of the shape of the specular peak for high glossy surfaces," Proc. SPIE - The Int. Soc. for Opt. Eng. **9018** (2014).